

JGR Solid Earth

RESEARCH ARTICLE

10.1029/2020JB021331

Key Points:

- Localized fracture can develop in initially ductile rocks due to pore fluid pressure increase
- Shear fracturing in the ductile rock is controlled by a brittle failure criterion and a critical dilatancy
- Injection rate controls the final fracture distribution

Supporting Information:

- Supporting Information S1

Correspondence to:

C. Noël,
corentin.noel@epfl.ch

Citation:

Noël, C., Passelègue, F. X., & Violay, M. (2021). Brittle faulting of ductile rock induced by pore fluid pressure build-up. *Journal of Geophysical Research: Solid Earth*, 126, e2020JB021331. <https://doi.org/10.1029/2020JB021331>

Received 11 NOV 2020

Accepted 18 FEB 2021

Brittle Faulting of Ductile Rock Induced by Pore Fluid Pressure Build-Up

Corentin Noël¹ , François X. Passelègue¹, and Marie Violay¹ 

¹Laboratory of Experimental Rock Mechanics, École Polytechnique Fédérale de Lausanne, Lausanne, Switzerland

Abstract Under upper crustal conditions, deformations are primarily brittle (i.e., localized) and accommodated by frictional mechanisms. At greater depth, deformations are ductile (i.e., distributed) and accommodated by crystal plasticity, diffusion mass transfer or cataclastic flow. The transition from the brittle to the ductile domain is not associated with a critical depth, but rather varies in time and space. One main parameter controlling the variation of this transition is the pore fluid pressure. On the one hand, a pore fluid pressure increase reduces the effective stresses and possibly increases the strain rate, bringing the system closer to brittle conditions. On the other hand, pore fluid can favor ductile mechanisms, mostly via chemical effects, by facilitating intra-crystalline plasticity, enhancing fluid-solid diffusion and fracture healing/sealing. We report triaxial laboratory experiments that investigated the effect of pore fluid pressure increase during the ductile deformation of Tavel limestone. Three injection rates were tested: 1, 5, and 10 MPa/min. We demonstrate that: (1) Under initially ductile conditions pore fluid pressure increase immediately turns the system from compaction to dilation. (2) Dilation is due to the development of localized shear fractures. However, the macroscopic localization of the deformation is not instantaneous when the ductile to brittle transition is surpassed; a transient creeping phase is first needed. (3) To reach macroscopic brittle failure of initially ductile samples, a critical dilatancy is required. (4) Injection rate controls the final fracture distribution. We demonstrate that pore pressure build-up in a rock undergoing ductile deformation can induce shear fracturing of the system.

1. Introduction

In the Earth's crust, irreversible deformations are usually accommodated by two distinct modes: brittle and ductile. Within the upper part of the crust, irreversible deformations are brittle and mainly localized along shear fractures (i.e., faults), limiting the rock strength to frictional and fracture motions (Paterson & Wong, 2005; Scholz, 2019). At greater depth, due to the increase of pressure and temperature, irreversible deformations are distributed, that is, ductile (Fredrich et al., 1989; Paterson & Wong, 2005; Scholz, 2019; Wong et al., 1997), and accommodated through plastic mechanisms such as mechanical twinning, dislocation creep (Evans et al., 1990), grain boundary diffusion/volume diffusion creep (Goetze & Brace, 1972; Rutter, 1986) or cataclastic flow (Wong & Baud, 2012). In this domain, the rock strength is described by flow laws sensitive to the temperature and deformation rate (Evans & Kohlstedt, 1995; Goetze & Brace, 1972; Goetze & Evans, 1979). Because rocks are polycrystalline materials, with each crystal having its onset of plastic deformation occurring under different conditions, the transition from brittle to ductile deformation with depth is intrinsically gradual. This transitional domain is called semi-brittle and involves the coexistence of both brittle and plastic deformation mechanisms (Fredrich et al., 1989; Meyer et al., 2019). This domain is of major importance as it marks the limit depth of seismicity (e.g., Sibson, 1977, 1982) and the limit of hydrothermal circuits in the crust (Violay et al., 2012, 2015, 2017). These two characteristics have led this domain to become of interest for deep reservoirs (e.g., Asanuma et al., 2012; Bignall & Carey, 2011; Frioleifsson et al., 2014; Tsuchiya et al., 2015).

Experimental studies of the brittle and ductile domains have led to a few simple constitutive laws meant to describe the deformation with a single mechanism (Evans & Kohlstedt, 1995; Lockner, 1995). These largely empirical laws are often derived from low-temperature tests on compact rocks (i.e., rocks with low porosity and without partial melts). In the brittle field, the empirical Coulomb failure criterion: $\tau = C + \mu' (\sigma_n - P_f)$, where τ is the shear strength, σ_n is the normal stress, P_f is the pore fluid pressure and μ' is the local slope of the failure criterion in the $\tau - \sigma_n$ space, remains the most used. However, theoretical formulations linking the remote stress applied to the rock sample to its internal damage have also been developed (e.g., Ashby &

Sammis, 1990; Costin, 1983, 1985; Sammis & Ashby, 1986). The most used is the *wing-crack model* developed by Ashby and Sammis (1990). In this model, that considers the initiation of the rock damage from inclined penny shape cracks, the strength of the rock depends on the applied confining and pore fluid pressures as well as some material parameters (i.e., initial damage, fracture toughness and frictional parameters). In the ductile field, dislocation creep is often represented by a steady-state power law of Arrhenius type (Evans & Kohlstedt, 1995; Kohlstedt et al., 1995; Weertman, 1978): $\dot{\epsilon} = A(\sigma_1 - \sigma_3)^n \exp\left(-\frac{Q}{RT}\right)$, where A is a material constant, σ_1 and σ_3 are the maximum and minimum principal stresses, n is the stress exponent, Q is the activation energy, R the gas constant and T the temperature. Other laws exist to describe ductile deformation (see Evans & Kohlstedt, 1995); however, they are all linked to a single mechanism of deformation. Moreover, all these constitutive laws are rough generalizations that neglect the effects of important state variables such as fluid chemistry, pore geometry, rock alteration, and microstructural changes. Furthermore, in the semi-brittle domain where both brittle mechanisms, such as frictional sliding or micro-cracking, and plastic mechanisms coexist, recent micromechanical models have been described (e.g., Wei & Anand, 2008); however, they are used under very specific conditions, and no simple satisfactory constitutive law exists for general cases. In summary, laboratory measurements have shown that the transition from brittle to ductile deformation is favored by: (1) increasing the effective confining pressure, i.e. the difference between the confining and the pore fluid pressures $P_c - P_f$ (e.g., Fredrich et al., 1989; Paterson, 1958; von Kármán, 1911); (2) increasing the temperature (e.g., Heard, 1960; Tullis & Yund, 1977); (3) decreasing the strain rate (e.g., Rutter, 1972a; Tullis & Yund, 1980). Therefore, depending on the in-situ conditions, the transition from brittle to ductile deformations is not related to a critical depth but varies with time and space (e.g., Handy et al., 2007).

One of the most important parameters that can move the brittle-ductile transition in time and space is the pore fluid pressure. Under ductile conditions, a pore fluid pressure increase can be related to natural causes (e.g., magma build-up in volcanic edifices, magmatic fluid pulses or fluid release during mineral phase changes) or to anthropogenic causes (e.g., for geo-energy purposes). Around the brittle-ductile transition, such pore fluid pressure variations may have a significant impact on the rock mass mode of deformation. On the one hand, pore fluid pressure variations can act as a catalyst for brittle deformation by: (1) reducing the effective confining pressure, bringing the mass rock closer to the brittle domain, particularly under drained conditions (Bernabe & Brace, 1990; Handin et al., 1963; Robinson, 1959; Rutter, 1972b); and (2) increasing the strain rate if rapid variations of the pore fluid pressure are produced (e.g., Noël et al., 2019a, 2019b). On the other hand, pore fluid can promote ductile deformations through chemically activated mechanisms by: (1) inhibiting the internal fracture of individual grains, allowing for intra-crystalline plasticity (Griggs, 1967; Heard, 1960; Rutter, 1972b); (2) enhancing fluid-solid diffusion (e.g., Farver & Yund, 1991); and (3) favoring fracture healing and sealing (e.g., Renard et al., 2000; Tenthorey et al., 2003).

Despite its importance for the brittle-ductile transition, only rare experimental studies have investigated the effect of increasing pore fluid pressure from the ductile domain toward the brittle domain. For example, Schubnel et al. (2006) showed that brittle deformations are favored in marble deforming under initially ductile conditions as a result of an effective confining pressure reduction. Additionally, Ougier-Simonin and Zhu (2013) showed that in porous sandstone, under initial conditions favoring ductile deformation of the sample (i.e., at an effective confining pressure of 70 MPa), increasing the pore fluid pressure from 10 to 18 MPa promotes strain localization.

In this study, we report new results from laboratory triaxial deformations performed under ductile conditions on a porous limestone. Particularly, we investigated the effect of an increase of pore fluid pressure on the transition toward the brittle domain, as well as the effect of the injection rate on ductile-brittle transitions.

2. Experimental Methodology

2.1. Starting Sample

Tavel limestone (North-West of Avignon, France) was used as a starting sample for the triaxial tests. It is almost 100% calcite and mainly composed of micrite particles of about 5 μm diameter cemented together (Nicolas et al., 2016, 2017; Vajdova et al., 2004, 2010; Vincké et al., 1998). Microscope analysis (with optical

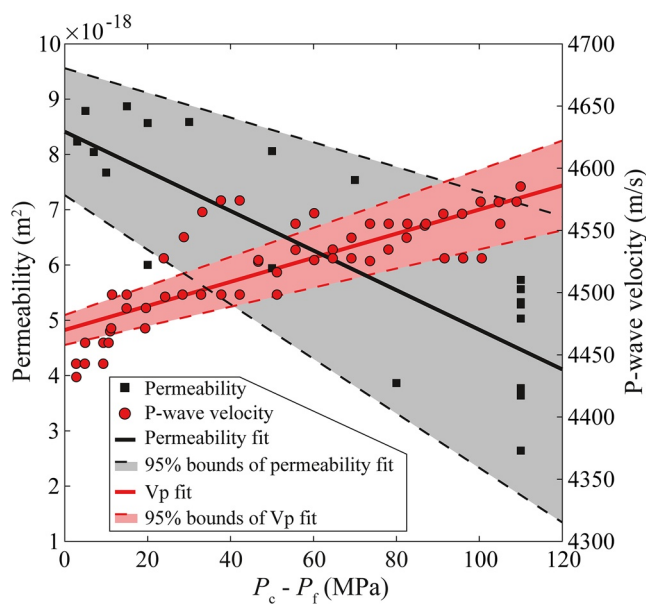


Figure 1. Permeability (k) and ultrasonic P-wave velocity (V_p) as a function of the effective confining pressure ($P_c - P_f$) of the Tavel limestone. Permeability data as a function of $P_c - P_f$ were fitted by a linear regression: $k = 3.58 \times 10^{-20} (P_c - P_f) + 8.41 \times 10^{-18}$ (full black line). V_p data as a function of $P_c - P_f$ were fitted by a linear regression: $V_p = 0.968 (P_c - P_f) + 4,470$ (full red line). The dotted black and red lines present the 95% interval bounds of the linear regressions of the permeability and V_p data, respectively.

Permeability of the samples was measured using the steady state Darcy flow method (i.e., by imposing a constant pore fluid pressure difference between sample ends and waiting for steady state flow to take place) under hydrostatic conditions at effective pressures ($P_c - P_f$) between 1 and 110 MPa. The samples showed a very slight decrease of the permeability with increasing hydrostatic effective pressure from 9×10^{-18} to $2 \times 10^{-18} \text{ m}^2$ (Figure 1). This low pressure dependence of the permeability suggests that the porosity contributing to the transport properties are mainly equant pores (Pimienta et al., 2017). Note that recent studies have shown that the effective stress coefficient for permeability can be higher than 1 for micritic limestone (e.g., Wang et al., 2018), possibly resulting in slightly lower permeability at elevated pore fluid pressure.

Ultrasonic P-wave velocities (V_p) were measured across the sample under hydrostatic conditions at ($P_c - P_f$) between 3 and 110 MPa (Figure 1). The samples show a slight increase from $4,410 \pm 45$ to $4,580 \pm 55 \text{ m.s}^{-1}$ with effective confining pressure. These measurements are in agreement with Nicolas et al. (2016) who found that V_p increases from $4,135$ to $4,350 \text{ m.s}^{-1}$ with increasing P_c from 0 to 85 MPa under dry conditions. The small variation of V_p with the applied effective pressure agrees with the small variation of permeability obtained.

2.2. Triaxial Deformations

2.2.1. Apparatus

Triaxial deformation experiments were performed using a conventional triaxial cell installed at the Laboratory of Experimental Rock Mechanics at the École Polytechnique Fédérale de Lausanne (Figure 2a). The system uses oil to apply a confining pressure ($P_c = \sigma_2 = \sigma_3$) up to 200 MPa ($\pm 5\text{-kPa}$ resolution). Upper and lower end platens are used to apply differential stress ($\sigma_1 - \sigma_3 = \sigma_1 - P_c = Q$) up to 1 GPa ($\pm 100\text{-kPa}$ resolution). The sample is isolated from the oil by a Viton jacket. Diffusion plates are placed at the sample ends to allow for a homogeneous pore fluid pressure distribution. Pore fluid pressure (P_f) is imposed with distilled water using step motor pumps, with a 185-cm^3 capacity, up to 200 MPa ($\pm 5\text{-kPa}$ resolution). The pore fluid pressure is

and scanning electron microscopes) of the sample revealed that its porosity is composed mainly of micro-pores at the junction between micritic particles and by a small number of more or less spherical macropores with diameters ranging from about 5 to 50 μm , consistent with previous pore analyses by Zhu et al. (2010). A detailed microscopic description of Tavel limestone can be found in Vajdova et al. (2010) and Zhu et al. (2010). This particular limestone has been chosen because calcite is capable of deforming plastically under room temperature and relatively low confining pressure conditions, facilitating experimental work. Moreover, its measured permeability (see details below) allowed for fluid injection under drained conditions.

Cores of Tavel limestone were diamond drilled from a unique block to a diameter of 36.5 mm. From the cores, 75 mm cylinders were sawed and the opposite faces ground flat with a parallelism of $\pm 100\text{-}\mu\text{m}$ precision. Tap water was used as cooling fluid for all the preparation steps. The samples were then petro-physically characterized and used for the triaxial tests.

Porosity of the samples was measured using the triple weight method (see Guégan & Palciauskas, 1994) and from the dry density of the samples assuming they are composed of 100% calcite. Using these two methods, similar porosity values were found: $10.6\% \pm 0.5\%$ and $10.8\% \pm 0.5\%$, respectively. Therefore, the porosity can be consistently considered as connected. The measured porosity is equivalent to the one found by Vajdova et al. (2004) and Vajdova et al. (2010), who found porosities of 10.4% and 10.6%, respectively, and lower than the one found by Nicolas et al. (2016), who measured a porosity of 14.7%.

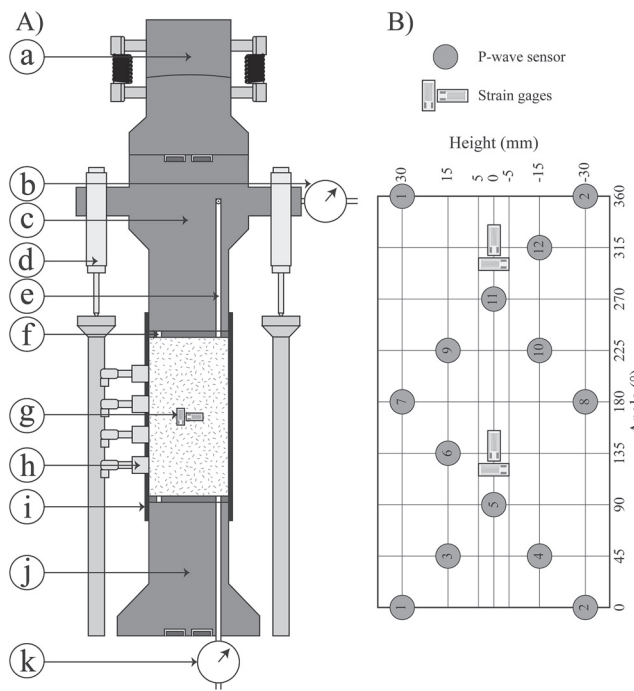


Figure 2. (a) Cross-section drawing of the assembly used for triaxial experiments. (a) ball joint to prevent sample misalignment, (b) upstream pore fluid pressure sensor, (c) upper end platen, (d) internal LVDT, (e) pore fluid lines, (f) drainage grooves to ensure homogeneous pore fluid pressure distribution, (g) strain gages, (h) piezo-electric sensor glued on the sample, (i) Viton jacket, (j) lower end platen and (k) downstream pore fluid pressure sensor. (b) Map of the acoustic sensors and strain gages used for injection experiments. Gray circles represent the position of the P-wave sensors and rectangles the position of the strain gages.

displacement rate at the internal LVDTs of $7.5 \times 10^{-5} \text{ mm.s}^{-1}$, which corresponds to a strain rate $\dot{\epsilon}_{\text{ax}} \approx 10^{-6} \text{ s}^{-1}$. The sample was then deformed up to the brittle failure of the specimen (i.e., to a stress drop), or up to

recorded by two precision pressure sensors ($\pm 5\text{-kPa}$ resolution) close to the sample ends. Pump fluid volume (V_f) variations are measured by encoders mounted on the pumps ($\pm 1\text{-mm}^3$ resolution). Axial displacements are measured using two internal Linear Variable Differential Transformers (LVDTs) with a precision of $1\text{ }\mu\text{m}$ and one external LVDT at the top of the axial column with a precision of $3\text{ }\mu\text{m}$. In addition, two axial and two radial strain gages were glued on the sample (Figure 2b), allowing for the monitoring of local strain during sample triaxial deformation, up to a maximum strain of 2%. Finally, the measurement of the evolution of elastic wave velocities during the triaxial experiments was conducted using 12 piezo-electric sensors (equipped with piezo-electric crystals: PI ceramic PRYY + 0400, 5-mm diameter and 1 mm thick) glued directly on the sample through holes drilled in the jacket (Figure 2Ah), which was resealed with ductile epoxy to prevent the intrusion of the confining oil into the sample. For these active velocity surveys, the emitted signals were pulsed at 450 V, and the received signals were amplified to 50 dB using a preamplifier and recorded at a 10-MHz sampling rate. The sensor arrangement was made so that the P-waves velocity could be measured at 30.9° , 50.2° , and 90° from the axis of the sample (Figure 2b), allowing for P-wave velocity anisotropy analysis during sample deformation.

2.2.2. Constant Pore Fluid Pressure Experiments

After placing the sample into the jacket and inserting it into the high-pressure vessel, the confining pressure was raised to 5 MPa. The sample was then pumped down to vacuum and 2 MPa of pore fluid pressure was applied at the bottom of the sample. Once the pore fluid was equilibrated (i.e., once P_f measured at the top reached 2 MPa and V_f was constant), the confining pressure and pore fluid pressure were increased simultaneously to their target values. For these experiments, the confining pressures ranged from 30 to 120 MPa and the pore fluid pressure was maintained constant at 10 MPa during the entire experiment (Table 1). When V_f was equilibrated, the axial stress was increased by applying a slow constant

displacement rate at the internal LVDTs of $7.5 \times 10^{-5} \text{ mm.s}^{-1}$, which corresponds to a strain rate $\dot{\epsilon}_{\text{ax}} \approx 10^{-6} \text{ s}^{-1}$. The sample was then deformed up to the brittle failure of the specimen (i.e., to a stress drop), or up to

Table 1
Summary on the Experimental Conditions and Triaxial Mechanical Data Performed on Tavel limestone.

Sample	P_c (MPa)	P_f (MPa)	P_f Conditions	E (GPa)	$(\sigma_1 - \sigma_3)$ at D'	(MPa)	$(\sigma_1 - \sigma_3)$ peak	(MPa)	$(\sigma_1 - \sigma_3)$ at C*	(MPa)	Failure angle (° from σ_1)	Post-mortem macro-deformation
TH5	30	10	Constant	48.5	170.2		189.4		-		22	Shear failure
TB5	60	10	Constant	41.5	208.0		215.8		-		33	Shear failure
TH6	90	10	Constant	48.3	266.9		306.5		92.9		31	DCSZ
TH2	120	10	Constant	44.4	-		-		122.4		-	Barrel shape
TB2	120	10	1 MPa.s^{-1}	45.9	-		-		116.6		22	Shear failure + DCSZ
TB9	120	10	1 MPa.s^{-1}	44.63	-		-		87.2		25	Shear failure + DCSZ
TB7	120	10	5 MPa.s^{-1}	43.1	-		-		87.8		22	Shear failure + DCSZ
TB4	120	10	5 MPa.s^{-1}	35.2	-		-		104.7		30	Shear failure + DCSZ
TH9	120	10	5 MPa.s^{-1}	45.7	-		-		96.4		23	Shear failure + DCSZ
TB8	120	10	10 MPa.s^{-1}	38.3	-		-		85.82		24	Shear failure + DCSZ
TH8	120	10	10 MPa.s^{-1}	46.3	-		-		101.5		23	Shear failure + DCSZ

DCSZ stands for distributed conjugated shear zone.

about 10% of its initial length for the experiments conducted in the ductile domain. Note that the strain rate was slow enough to maintain drained conditions in the sample during the deformation (i.e., upstream $P_f \approx$ downstream P_f , consistent with diffusion time computed by Nicolas et al. (2016)).

2.2.3. Injection Experiments

For the injection experiments, the same initial procedure was applied as for the constant pore fluid pressure experiments. The initial confining pressure and pore fluid pressure were set to $P_c = 120$ and $P_f = 10$ MPa (ductile domain, see Section 3.1). After 1% of axial deformation, the pore fluid pressure was raised gradually at the bottom of the sample up to 100 MPa (i.e., $P_c - P_f = 20$ MPa). Note that at equivalent $P_c - P_f$, the axial stress and the volumetric strain are directly linked ($\varepsilon_{vol} = \varepsilon_{ax} + 2\varepsilon_{rad}$), therefore the injections are considered to start at equivalent volumetric strain. 100 MPa pore fluid pressure limit was chosen to prevent leakage from the P_f to the confining oil. Three pore fluid pressure rates were tested: 1, 5, and 10 MPa·min⁻¹ (Table 1). The mechanical deformation of the sample was stopped when the sample reached an axial strain of 2%. During sample deformation, active P-wave velocity surveys were made every 2 min. Note that during the full length of the injection experiments, the velocity of 7.5×10^{-5} mm·s⁻¹ (i.e., $\dot{\varepsilon}_{ax} \approx 10^{-6}$ s⁻¹) at the LVDTs continues to apply.

2.3. Data Treatment and Analysis

For each experiment, the displacement measured from the LVDTs was corrected for the elastic distortion of the apparatus column (i.e., axial column, end platens and diffusion plates for the external LVDT and end platens and diffusion plates for the internal LVDTs), calibrated using a metal plug of a known stiffness. For all the experiment, the differential stress was corrected for the friction of the axial piston in the apparatus column. For each experiment, the axial strain (ε_{ax}) was computed as the ratio between the corrected axial displacement and the initial sample length. The porosity change was computed as the ratio between the injected pore fluid volume (V_f) and initial bulk volume of the sample. Note that for the injection experiments, the porosity change was calculated by correcting the pore fluid volume linked to the pore pressure increase (i.e., due to the dilation of the pore fluid lines and water compressibility). Finally, the volumetric strain (ε_{vol}) was computed using the local measurement of the strain recorded on axial and radial strain gages assuming $\varepsilon_{vol} = \varepsilon_{ax}^{SG} + 2\varepsilon_{rad}^{SG}$, with ε_{ax}^{SG} and ε_{rad}^{SG} being the axial and radial strain measured by the strain gages, respectively. Importantly, strain gages allow for very local strain measurements such that localized deformations are often not measured by the strain gages, leading to volumetric strain underestimation in the case of large strain localization. However, overestimations are also possible if localized deformations occur at the location of the strain gages.

For each experiment, the P-wave velocities (V_p) obtained from the active surveys were corrected by the elastic effective pressure dependence (Figure 1). This allowed for the removal of the poroelastic response of the bulk due to the increase of the pore fluid pressure. We note this corrected P-wave velocity as $V_p^{\text{corrected}}$. In order to remove sample variability, the values of $V_p^{\text{corrected}}$ are then normalized by the initial values (V_{p0}) measured at $P_c - P_f = 110$ MPa before the application of the differential stress. In addition, the computed $V_p^{\text{corrected}}$ along the different pathways were used to invert the evolution of the average corrected crack densities's increase during the experiment. This inversion was performed in the framework of a transversely isotropic crack distribution, following standard procedure (see Sarout & Guéguen, 2008a; 2008b). The minimization of the difference between the theoretical and the experimental wave velocities was conducted using a least absolute method for each velocity survey. The inversion outputs the best solution for the transversely isotropic stiffness tensors from which the average crack densities (independent of their orientation form the principal stresses) are computed. Here, we computed the evolution of the crack density using $V_p^{\text{corrected}}$ instead of the absolute V_p values, to remove the poroelastic effects due to the increase of fluid pressure (like the opening of cracks inducing loss of contacts along the crack). Note that this method considers the cracks to be under dry conditions, therefore, in the case of a saturated sample, it leads to an underestimation of the crack densities. The crack densities estimated in the following correspond to the average crack densities for all possible orientations, which is computed from both vertical (α_v) and horizontal (α_h) crack densities assuming $\rho_{tot} = 2\alpha_v + \alpha_h$.

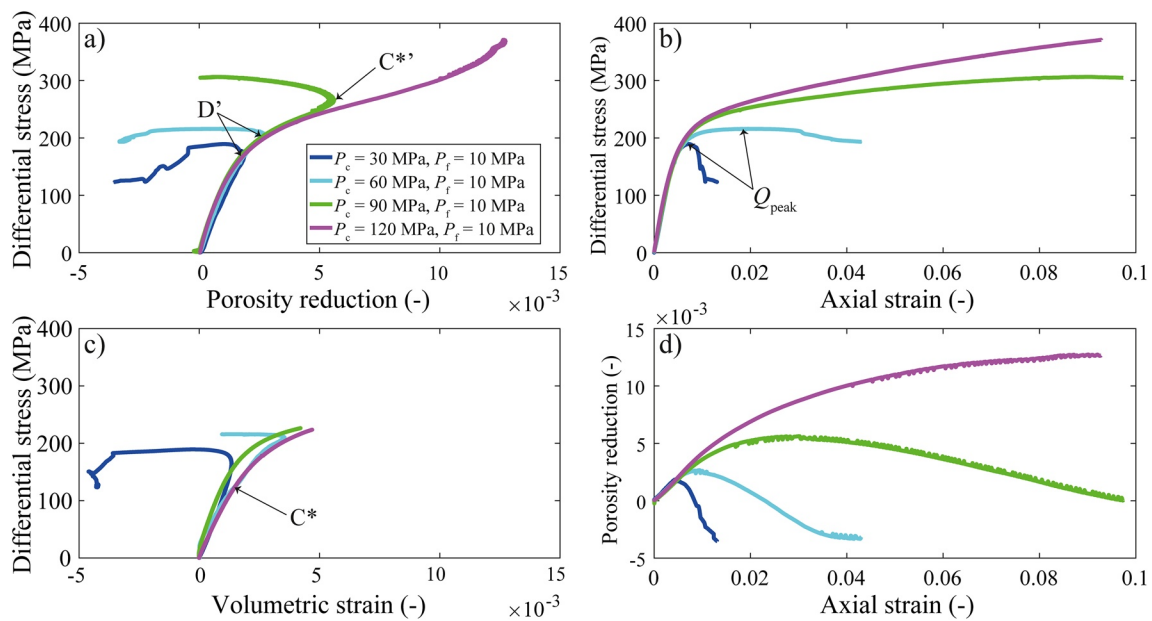


Figure 3. Mechanical data obtained from Tavel limestone deformed at $P_c - P_f$ ranging from 20 to 110 MPa. (a) Differential stress ($\sigma_1 - P_c$) as a function of the porosity reduction. (b) Differential stress as a function of the axial strain. (c) Differential stress as a function of the volumetric strain. (d) Porosity reduction as a function of the axial strain. Note that the volumetric strain could not be recorded at values higher than 0.5% due to the system limitation.

After samples deformation, each sample was carefully taken out of the jacket. If a macroscopic shear failure had occurred, its angle from the sample axis (i.e., equal to the orientation of σ_1) was measured. Then, samples were impregnated with epoxy under vacuum and a thin section perpendicular to the macroscopic structural deformation (if visible) was prepared and analyzed under optical and scanning electron microscopes (SEM) in secondary electron mode.

3. Results

3.1. Constant Pore Fluid Pressure Experiments

Constant pore fluid experiments were performed to characterize the short-term mechanical behavior of Tavel limestone and to constrain its brittle-ductile transition. The mechanical results (Figure 3 and Table 1) serve as reference for the injection experiments. For the confining pressures tested, three mechanical behaviors were observed:

- (1) For experiments performed at $P_c - P_f \leq 50$ MPa, after an initial linear increase of the differential stress ($\sigma_1 - P_c$) with the axial strain, the onset of dilatancy is reached and the curve departs from linearity. After the elastic deformation, the sample exhibits a strain hardening behavior up to a peak value (Q_{peak} i.e., sample strength). During this phase, the deformation turns from compaction to dilation at the point denoted D' (Figure 3a and 3c). Following this peak, the sample enters a strain softening phase after which the stress remains at a quasi-constant residual strength up to the end of the deformation.
- (2) For experiments performed at $P_c - P_f \geq 110$ MPa, after a first linear increase of the differential stress with the axial strain and the volumetric strain, the mechanical curves deviate from linearity at a point noted C* (Figure 3). After this point, the sample follows a nonlinear hardening phase. Finally, a constant hardening rate is reached and the differential stress—axial strain curve again presents a linear behavior (Figure 3b). During the entire experiment, the sample deformation is accommodated by compaction (Figure 3a and 3d).
- (3) For the experiment performed at $P_c - P_f = 80$ MPa, a mix between the two behaviors was observed. After an elastic behavior, the deformation becomes nonlinear and the sample exhibits strain hardening. Then, a quasi-linear strain hardening behavior is observed. During this phase, the sample first

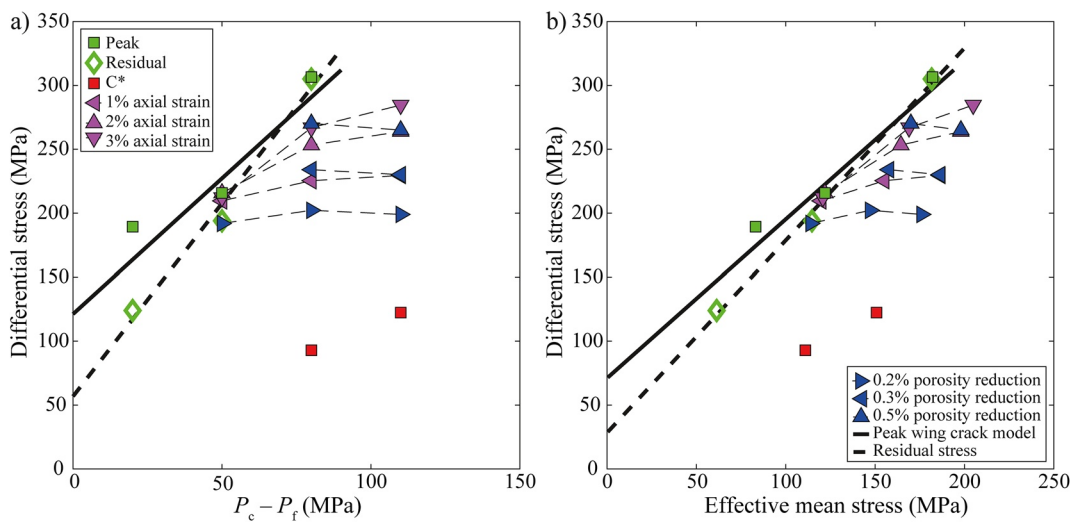


Figure 4. Peak differential stress, residual strength, differential stress at C^* , differential stress at 1%, 2%, and 3% of axial strain and differential stress at a porosity reduction of 0.2%, 0.3%, 0.5% obtained from the constant pore fluid pressure experiments performed on Tavel limestone, plotted as a function of (a) the effective confining stress and (b) the effective mean stress. Peak differential stress data are fitted with a wing crack model (Ashby & Sammis, 1990), with an initial flow size of $0.8 \mu\text{m}$ oriented at 45° from the axial stress, a coefficient of friction of 0.6, a critical stress intensity factor of $0.2 \text{ MPa} \cdot \text{m}^{1/2}$, and an initial damage of 0.3 (similar to Vajdova et al., 2004). Residual stress data are fitted linearly with $Q_{\text{residual}} = 3.02 \times (P_c - P_f) + 56.8$. See supplementary materials for more details on the parameters used in the models.

compacts. After an axial strain of about 2.8%, dilatancy become dominant at a point denoted C^* (Figure 3a). After an axial strain of about 7%, the strain hardening decreases and a peak differential stress is ultimately reached at an axial strain of 9.05% (Figure 3b). Finally, the sample enters a very small strain softening phase.

The peak differential stress, the residual strength of experiments in the brittle field, as well as the differential stress at C^* of the experiments in the ductile field were extracted to build the failure/damage envelope of Tavel limestone (Figure 4). The values of differential stress observed at 1%, 2%, and 3% of axial strain and at 0.2%, 0.3%, and 0.5% of porosity reduction are reported for experiments devoid of macroscopic stress drop during the early stage. Two envelopes were defined for the brittle field using the wing crack model to fit the sample strength (Ashby & Sammis, 1990; Brantut et al., 2012, black line in Figure 4a) linear regression to fit the residual strength (black dashed line in Figure 4).

More details on the mathematical formulations and parameters used for the envelopes are presented in the supplementary materials.

The post-mortem analyses of the samples showed that, for samples deformed at $P_c - P_f \leq 50 \text{ MPa}$, the deformation was mainly localized along anastomosed shear fractures with orientations ranging between 22° and 31° from σ_1 (Table 1 and Figure 5b, 5f, and 5i). Microscopic analysis revealed that micro-cracking is the main mechanism controlling the deformation, although twinning was also observed (Figure 5f). The formation of these opened cracks is in agreement with the dilation observed during the sample deformation. The post-mortem samples deformed at $P_c - P_f \geq 110 \text{ MPa}$ present a barrel shape, and the deformation is distributed across the sample (Figure 5d, 5h, and 5k). Microscopic analysis revealed that grains endured mechanical twinning and distributed micro-cracking (Figure 5h). Some macro-pores present ovoid shapes flattened perpendicularly to σ_1 (Figure 5h and 5k). Finally, the samples deformed at $P_c - P_f = 80 \text{ MPa}$ showed both a deformation that occurred distributed across the sample (i.e., barrel shape) and a localized deformation along discreet shear fractures, that is, noncontinuous fractures of finite length ranging from 0.5 to 2 mm (Figure 5c, 5g, and 5j). Microscopic analysis revealed multiple noncontinuous shear fractures with small apertures forming discreet shear zones (Figure 5g and 5j). Additionally, distributed microcracking and twinning were present.

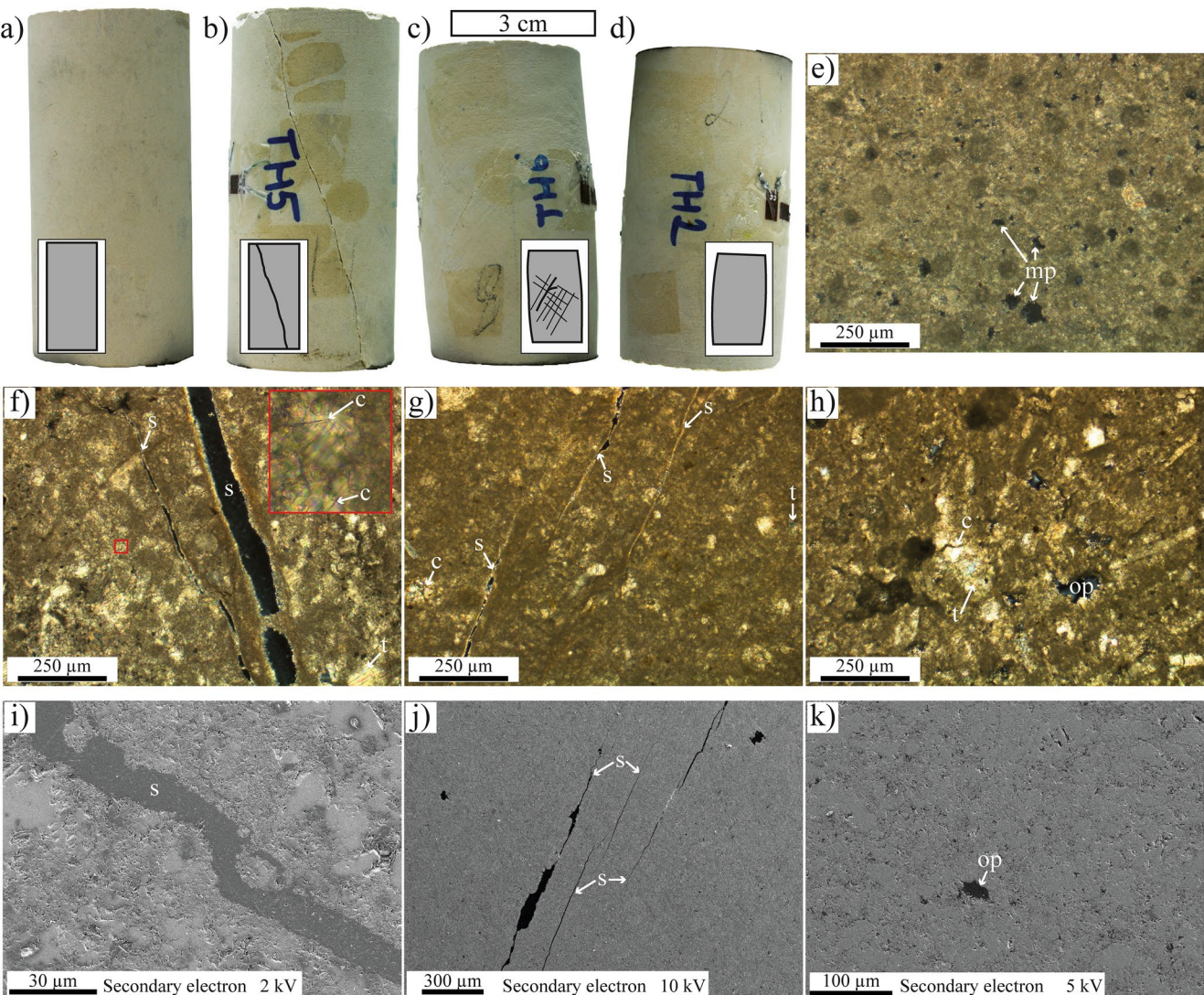


Figure 5. Post-mortem analysis of the samples which were deformed under constant pore fluid pressure conditions. (a–d) Macroscopic photo with schematic representation. (e–h) Micrographs taken under a cross-polarized microscope. (i–k) SEM image in secondary electron mode. (a and e) intact sample. (b, f, and i) sample deformed in the brittle domain (i.e., at $P_c - P_f \leq 50$ MPa) by shear fracturing. (c, g, and j) sample deformed at the brittle-ductile transition (i.e., at $P_c - P_f = 80$ MPa). (d, h, and k) sample deformed in the ductile domain (i.e., at $P_c - P_f \geq 110$ MPa). For the micrographs (e–h), σ_1 is oriented subvertically. For the SEM images (i–k), σ_1 is oriented subvertically. A zoom on a highly cracked zone (red square) is presented in panel (f) Abbreviations: mp, macro-pore; s, shear fracture; c, crack; t, twinning; op, ovoid pore.

3.2. Injections Experiments

For the injection experiments, the evolutions of the mechanical and P-wave velocity behaviors (Figures 6–8) can be described in five steps. For reference, a typical mechanical behavior of an injection experiment as well as the stress path seen by the sample is shown in Figure 6. All the injection experiments presented the following steps:

- (1) Before pore fluid injection, all the samples presented a similar mechanical behavior, with a first linear elastic behavior followed by a hardening phase and compaction (Figures 6 and 7). During this phase, $V_p^{\text{corrected}}$ was constant (Figure 8). This primary behavior is similar to the experiments performed at $P_c - P_f = 110$ MPa under constant pore fluid pressure conditions (black line in Figure 7), and all the experiments present relatively similar differential stresses at C^* (i.e., 100.3 ± 13.8 MPa, Table 1). At the end of this stage, and just before the injection started, the samples porosity was reduced by 0.40%–0.45%.

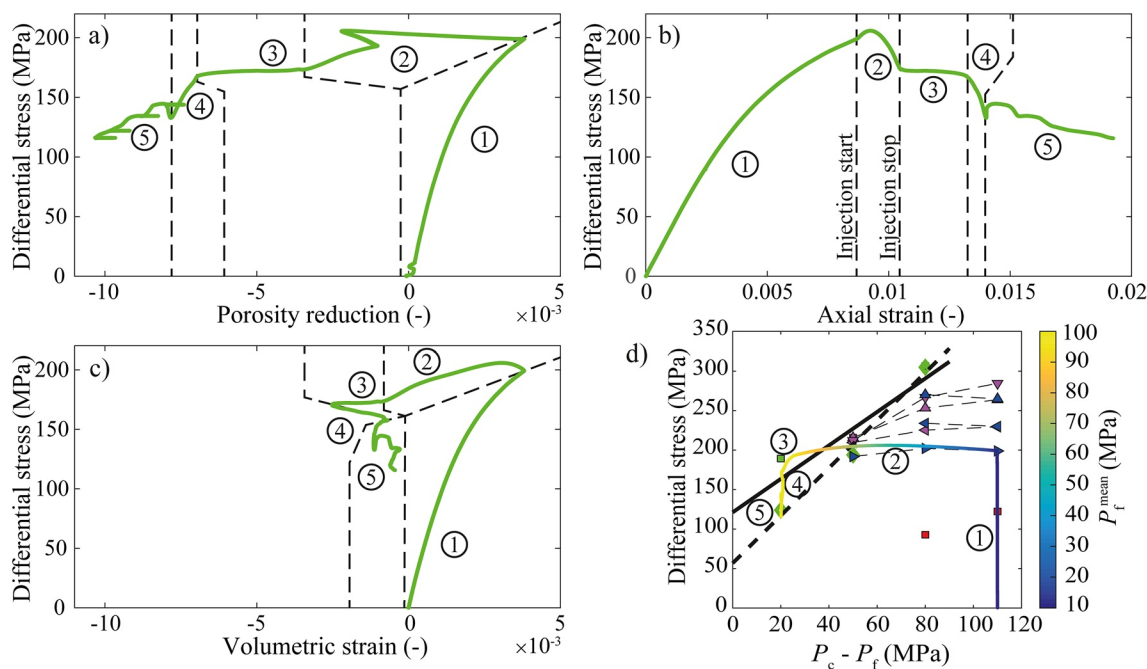


Figure 6. Mechanical data obtained for the injection experiments at 5 MPa/min on Tavel limestone. (a) Differential stress as a function of the porosity reduction. (b) Differential stress as a function of the axial strain. (c) Differential stress as a function of the volumetric strain. (d) stress path seen by the sample plotted over the summary of the mechanical data obtained in the constant pore pressure experiments (i.e., Figure 4). P_f^{mean} is the pore fluid pressure average between the upstream and downstream pore fluid pressure sensors. On the four panels, the numbers 1 to 5 refer to the five principal steps observed in injection experiments (see the main text for more details).

- (2) When injection started (at an axial strain of about 1%), all the samples passed instantaneously from compaction to dilation (Figures 6a, 6b, 7a, 7c, and 7d) and the hardening rate increased (Figures 6b and 7b). As the pore pressure rose, the hardening rate decreased and the differential stress reached a peak value after which softening was observed. These hardening and softening rate changes depended on the injection rate: the higher the injection rate, the smaller the axial strain was at the peak differential stress. Moreover, for all the experiments, the peak differential stress value was reached at $P_f \approx 50$ MPa (i.e., $P_c - P_f \approx 70$ MPa). Finally, the softening stopped when the injection reached the target value of $P_f = 100$ MPa (i.e., $P_c - P_f = 20$ MPa). During this phase, $V_p^{\text{corrected}}$ dropped quasi-linearly to between 95% and 85% of the initial value. Following the trends seen in V_p , the corrected crack density increases from about 0.05 to 0.1. Note that during the injections, the strain rate seen by the sample changes. For low injection rates (i.e., 1 MPa/min) the variations are negligible. For experiments with injection rates of 5 and 10 MPa/min, the strain rate slightly increased from 10^{-6} to 2.9×10^{-6} and $3.9 \times 10^{-6} \text{ s}^{-1}$, respectively. After the injection stopped, the strain rate quickly decreased back to 10^{-6} s^{-1} . Additionally, for high-injection rates (5 and 10 MPa/min) a pore pressure gradient was produced within the sample. The delay time to reach equilibrium was 3 min at maximum such that the experiments can be considered undrained during moments of large pressure gradient, and drained the rest of the time. As a consequence of this drainage issue, for the injection experiments at 5 and 10 MPa.min⁻¹, a “z-shape” is visible on the differential stress as a function of the porosity reduction curve close to the peak differential stress (Figures 6a and 7a). A “u-shape” is also visible on the porosity reduction as a function of the axial strain curve at an axial strain of about 0.9% (Figure 7d). These are not real porosity changes but artifacts of the correction methods (i.e., water diffusion delay).
- (3) When the injection stopped, the softening also stopped and the differential stress remained at a quasi-constant value with increasing the axial strain (i.e., creep phase). Interestingly, this constant differential stress corresponds to the peak differential stress observed during the constant pore pressure experiment performed at $P_c - P_f = 20$ MPa (i.e., the effective pressure reached for the injection experiments). During this quasiconstant differential stress phase, the samples continued to dilate (Figures 6a–6c and 7a–7c). The $V_p^{\text{corrected}}$ values continued to drop but with a shallower slope than during the previous phase (Fig-

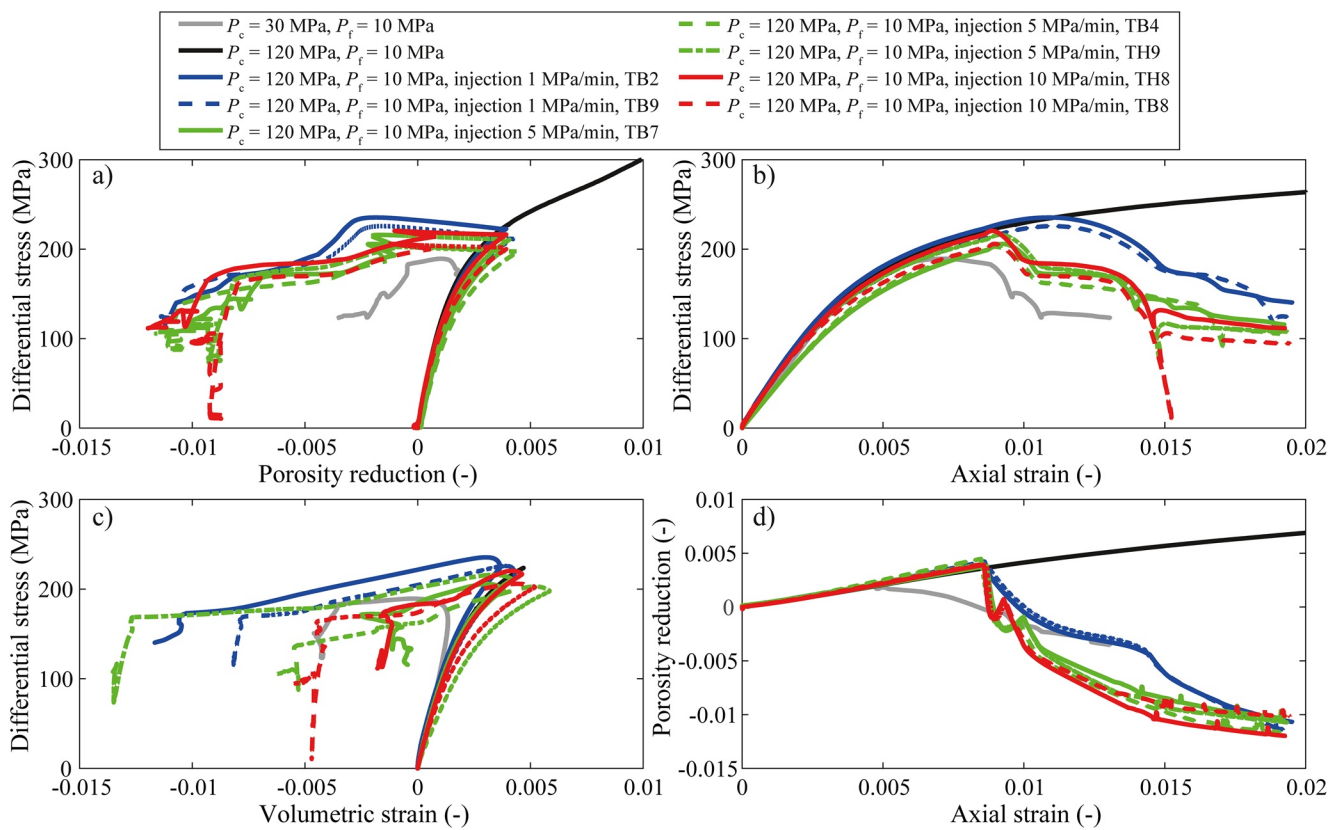


Figure 7. Mechanical data obtained for the injection experiments on Tavel limestone (colored curves). Constant pore fluid experiments at $P_c - P_f = 110$ and 20 MPa are also plotted for reference (black and gray curves, respectively). (a) Differential stress as a function of the porosity reduction. (b) Differential stress as a function of the axial strain. (c) Differential stress as a function of the volumetric strain. (d) porosity reduction as a function of the axial strain. The experiments performed with injection rates of 1, 5, and 10 $\text{MPa} \cdot \text{min}^{-1}$ are represented by blue, green and red colors, respectively. Note that for the injection experiments at 5 and 10 $\text{MPa} \cdot \text{min}^{-1}$, the “z-shape” and “u-shape” visible on the curves of differential stress as a function of porosity reduction (close to the peak differential stress) and porosity reduction as function of the axial strain (at about 0.9% of axial strain), respectively, are not real porosity changes but artifacts due to the correction methods (i.e., diffusion delay).

ure 8). Similarly, the corrected crack density continues to increase, albeit slower than during previous phase (Figure 8).

- (4) The creep phase ultimately led to a stress drop that marks the sample failure (Figures 6 and 7). Note that this stress drop occurred systematically when the porosity had increased by about 1%. The stress drop did not significantly affect the $V_p^{\text{corrected}}$ and corrected crack density values (Figure 8). Note that the stress drops were sometimes excessive due to the servo-control of the machine.
- (5) After the stress drop, a residual stress remained. The residual differential stress had similar values to the residual stress observed during the constant pore fluid pressure experiments performed at $P_c - P_f = 20$ MPa. After the stress drop, $V_p^{\text{corrected}}$ values remained constant at 92%–82% of the initial values. The corrected crack density also remains constant, at values between 0.1 and 0.15, depending on the sample.

Post-mortem analyses of the samples showed that all samples presented a principal anastomosed shear fracture oriented between 22° and 30° from σ_1 (Table 1 and Figure 9). Most of the samples also presented distributed discreet shear fractures oriented at 20° – 35° from σ_1 . However, increasing the injection rate from 1 to 10 $\text{MPa} \cdot \text{min}^{-1}$ reduced the number of these distributed shear fractures (Figures 9a–9c). Indeed, at low injection rates (i.e., 1 $\text{MPa} \cdot \text{min}^{-1}$), the macroscopic shear fracture is surrounded by discreet millimetric-to centimetric-scale fractures forming a wide deformation zone around the principal fault (Figures 9d, 9g, and 9j). For a medium injection rate (i.e., 5 $\text{MPa} \cdot \text{min}^{-1}$), the macroscopic fracture is wider and surrounded by a small amount of fractures of finite length (Figures 9e, 9h, and 9k). Finally, for high injection rates (i.e.,

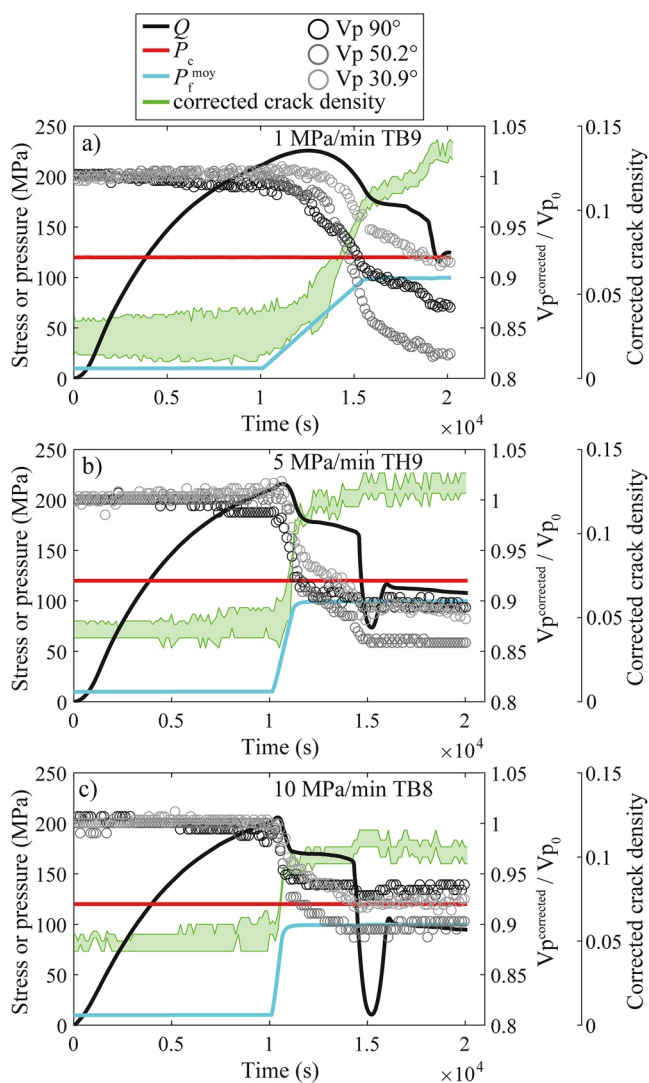


Figure 8. P-wave velocities at 90°, 50.2°, and 30.9° from σ_1 corrected for poroelasticity and normalized by the reference velocity (see Section 2.3 for precision) as a function of time. The computed corrected crack density values are shown in green. The green zone delimits the uncertainty of the computation. The differential stress, confining pressure and pore fluid pressure are represented by the black, red, and light blue curves, respectively. (a) Sample TB9 with an injection rate of $1 \text{ MPa} \cdot \text{min}^{-1}$. (b) Sample TH9 with an injection rate of $5 \text{ MPa} \cdot \text{min}^{-1}$. (c) Sample TB8 with an injection rate of $10 \text{ MPa} \cdot \text{min}^{-1}$. Note that the corrected crack densities are underestimated due to the method used (see Section 2.3 for more details).

mechanical data obtained (Figure 3). Indeed, at low-effective pressure, dilatant deformations are directly linked to micro-crack formation, whereas at high effective confining pressure compaction is related to mechanical twinning and pore deformation (i.e. with pore volume reduction by cataclastic pore collapse) (Zhu et al., 2010). The mechanical data (Figure 3) and microstructural analysis (Figure 5) demonstrate that Tavel limestone has a brittle-ductile transition around an effective confining pressure of 80 MPa at room temperature. This is in agreement with previously published data by Nicolas et al., (2016) and Vajdova et al., (2004) who observed a transition at 70 MPa and between 50 and 100 MPa effective pressure, respectively.

10 $\text{MPa} \cdot \text{min}^{-1}$), the macroscopic shear fracture is marked by three to four parallel fractures, and only few scattered cracks of finite length are present (Figures 9f, 9i, and 9l). In summary, the lower the injection rate, the more the macroscopic shear fracture is bounded by distributed fractures of finite length.

4. Interpretation and Discussion

The experiments performed in this study highlight that:

- (1) Tavel limestone exhibits a brittle-ductile transition at room temperature and an effective confining pressure around 80 MPa.
- (2) An increase of pore fluid pressure in a rock sample submitted to ductile conditions turns the system instantaneously to dilation.
- (3) The combination of the P-wave velocity decrease and sample dilation constrain the moment when localized shear deformation take place. The micro-cracking of the sample starts when the ductile-brittle transition is overcome. However, macroscopic failure is not instantaneous when the ductile-brittle deformation is passed. A transient creeping phase is necessary to achieve the macroscopic shear failure of the specimen.
- (4) To obtain a macroscopic brittle failure of initially ductile samples (marked by the stress drop), a critical dilatancy is required. Under our experimental conditions and strain rates, a dilatancy of about 1% was systematically needed to obtain shear fracturing.

In the following, we first discuss the brittle-ductile transition of Tavel limestone with increasing effective confining pressure. Then, we discuss and interpret the brittle deformations obtained during the ductile-to-brittle transition induced by an increase in the fluid pressure and compare them to the ones observed during constant fluid pressure experiments conducted through the transition. Finally, we discuss the implications of our experimental results for natural and induced deep seismicity.

4.1. Brittle-Ductile Transition With Increasing Effective Confining Pressure

To facilitate the discussion of the injection experiments, we summarize here the principal characteristics of the brittle to ductile transition in Tavel limestone and compare it with previous studies. The microstructural analysis (Figure 5) of the constant pore fluid pressure experiments show that Tavel limestone deformed by localized shear fractures at $P_c - P_f \leq 50 \text{ MPa}$, by discreet shear zones at $P_c - P_f = 80 \text{ MPa}$, and by distributed micro-cracking, mechanical twinning and macro-pore deformations at $P_c - P_f \geq 110 \text{ MPa}$. These observations agree with the

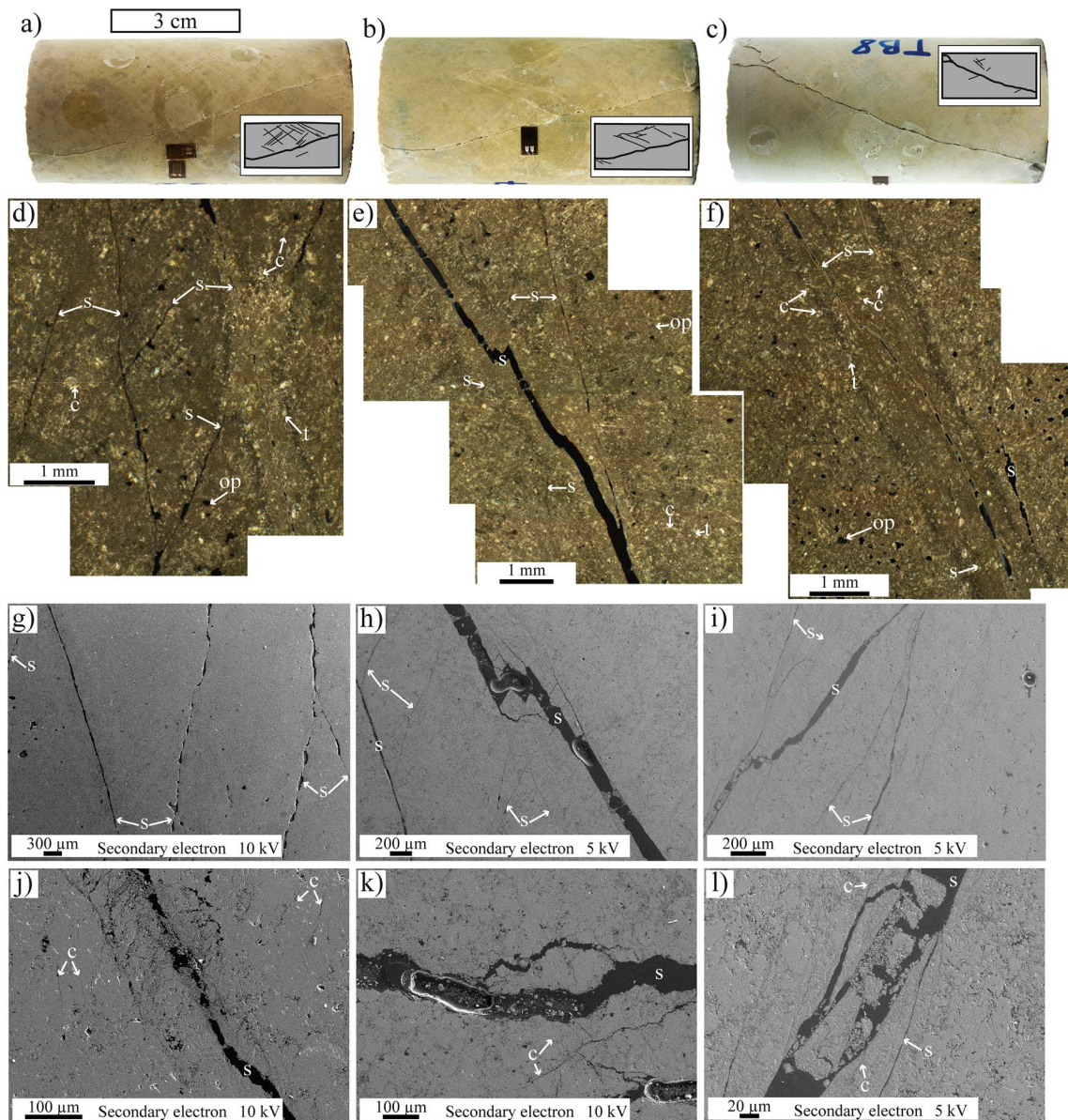


Figure 9. Injection experiment post-mortem analysis of the samples. (a–c) Macroscopic photo with schematic representation. (d–f) Mosaic of micrographs taken under cross-polarized microscope. g–l) SEM images in secondary electron mode. (a, d, g, and j) sample deformed with an injection rate of $1 \text{ MPa} \cdot \text{min}^{-1}$. (b, e, h, and k) sample deformed with an injection rate of $5 \text{ MPa} \cdot \text{min}^{-1}$. (c, f, i, and l) sample deformed with an injection rate of $10 \text{ MPa} \cdot \text{min}^{-1}$. For these micrographs, σ_1 is oriented vertically. Note that the panels magnifications are different. Abbreviations: s, shear fracture; c, crack; t, twinning; op, ovoid pore.

Interestingly, the brittle-ductile transition occurs at the point where the strength (i.e., Q_{peak}) and the residual friction envelopes cross (full and dotted black lines in Figure 4). This characteristic has been observed previously (e.g., Barton, 1976; Byerlee, 1968; Maurer, 1965; Mogi, 1974; Murrell, 1967). Experimental data showed that the fracture strength of the material is less pressure dependent than frictional strength (e.g., Paterson & Wong, 2005) (Figure 4). Therefore, under high effective pressure, it is assumed that nonfrictional deformation mechanisms are more efficient than frictional ones, leading to distributed deformation. Indeed, considering the ideal case of a rock deforming in the brittle field by wing cracks emanating from sharp sliding inclined cracks (i.e., wing crack model), if crack sliding is avoided by the pressure effect, coalescence of micro-cracks will be prevented, and other mechanisms of deformation will be favored (i.e., cracks nucleating from other discontinuities, mechanical twinning, pore collapse, etc.). This allows for the brittle-ductile transition to be overcome through an increase in the effective confining pressure.

4.2. Ductile to Brittle Deformation Induced by Pore Pressure Increase

The injection experiments performed showed that an initially ductile rock mass can undergo localized shear fracturing (i.e., brittle deformations) due to pore fluid pressure increase. Previous experiments on Carrara marble by Schubnel et al. (2006), led to an equivalent result. Indeed, lowering the effective confining pressure from 120 to 5 MPa by means of pore fluid pressure increase, caused the brittle failure of the sample that was initially deforming in the ductile domain. Similar results were obtained by Ougier-Simonin and Zhu (2013) when increasing the pore fluid pressure from 10 to 18 MPa during the deformation of Berea sandstone at $P_c = 80$ MPa. Under the initial conditions they tested (i.e., $P_c - P_f = 70$ MPa), Berea sandstone is in a transitional regime between brittle faulting and cataclastic flow. Increasing the P_f by 8 MPa was enough to cause localized shear failure of the sample. Together, these results demonstrate the importance of pore fluid pressure variation on the ductile to brittle transition.

The obtained results add new constraints on the role and the mechanical effect of pore fluid pressure increase in a system that deforms in an initially ductile manner:

- (1) While deformation was primarily compactant in the ductile regime, samples underwent immediate dilation when the pore fluid pressure was raised (Figure 7). V_p data can be used to better understand what happened in this primary phase. Indeed, using V_p data and the inferred corrected crack density, one can approximate the microstructural deformations at hand. By correcting V_p data for the initial poroelastic response (see Section 2.3), we were able to discriminate between the elastic opening of the existing crack (i.e., constant $V_p^{\text{corrected}}$) and new micro-cracks formation/elongation (i.e., drop of the $V_p^{\text{corrected}}$). In general, $V_p^{\text{corrected}}$ data were dropping immediately after the pore fluid pressure was increased. Consistent with the velocity data, the computed corrected crack density immediately increased when the pore fluid pressure was raised. This led us to infer that immediate dilation of the sample was due to micro-crack formation.
- (2) We also demonstrated that the macroscopic failure of the sample is not instantaneous when the ductile-brittle transition is passed. First, a softening phase occurred up to the moment we reached the target P_f of 100 MPa. Then, a transient creep phase, corresponding to the sample strength at equivalent effective confining pressure, was needed before failure. During this creep phase dilation increased up to about 1% prior to failure. Again, using V_p and corrected crack density data, we can differentiate two distinct phases of $V_p^{\text{corrected}}$ decrease and corrected crack density increase during the injection experiments: a first fast $V_p^{\text{corrected}}$ decreasing phase during the pore fluid pressure increase and a second slower decreasing phase during the creep phase (Figure 8). These two phases can also be distinguished on the corrected crack density with two different increasing slopes. We can thus infer that while the pore fluid pressure was increased (i.e., the first, fast phase of $V_p^{\text{corrected}}$ decrease and corrected crack density increase) micro-cracking was intense. However, once the target pore fluid pressure of 100 MPa was reached, the micro-cracking state of the sample was not enough to result in coalescence. Therefore, a creeping phase occurred, during which micro-cracks continued their nucleation and propagation (i.e., the second, slower phase of $V_p^{\text{corrected}}$ decrease and corrected crack density increase). Once the micro-crack density was high enough (i.e., in the case of Tavel limestone at 1% dilation), coalescence occurred and the sample macroscopically failed under shearing. The inferred two phases of fast then slower micro-crack density increase agree with the two phases of faster and then slower porosity increase (Figures 7a and 7d). This result is in agreement with previous observations in the brittle field where a critical dilatancy is needed before the onset of macroscopic shear failure (Kranz & Scholz, 1977). Previous experimental and field studies that measured P-wave velocity during rock or fault macroscopic shear failure (i.e., stress drop) have shown that V_p slightly decreases prior to and during shear failure (e.g., Kaproth & Marone, 2013; Niu et al., 2008; Scuderi et al., 2016; Shreedharan et al., 2021; Taira et al., 2015). Here, such variation could not be measured during the sample macroscopic shear failure due to the large interval between two V_p measurements (i.e., every 2 min, while stress drop is quasi-instantaneous). Note that the crack densities estimated at the failure of the specimens are smaller than the percolation threshold (i.e., critical crack density) for failure observed in previous studies (i.e., ≈ 0.13 rather than 0.3) (e.g., Passelègue et al., 2018; Wang et al., 2013). This is probably related to an underestimate of the crack density in fluid saturated media, as observed in previous studies (e.g., Sarout & Guéguen, 2008a; 2008b).

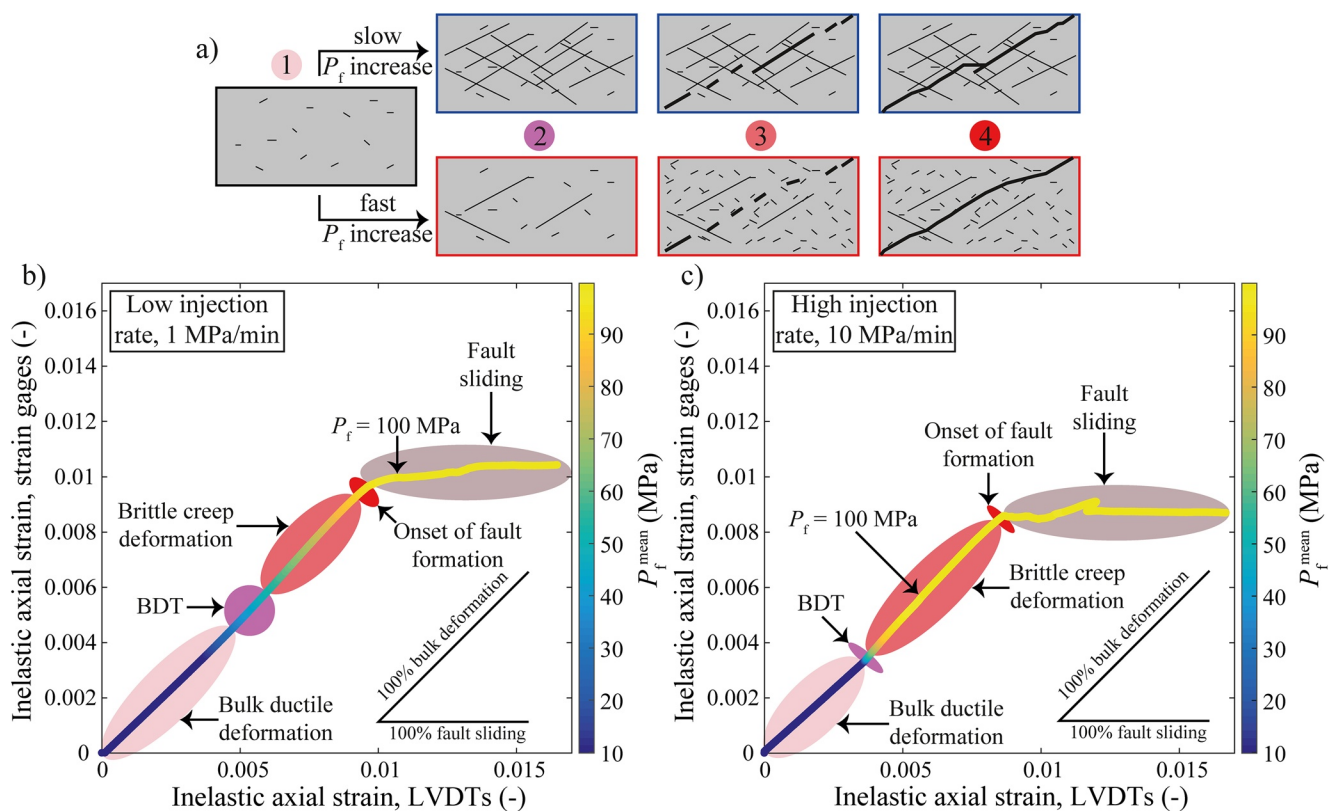


Figure 10. (a) Conceptual microscopic model of the deformations occurring during fluid injection into a ductile rock mass. Step 1 represents the bulk ductile deformations. Step 2 represents the ductile-brittle transition. Step 3 represents the brittle creep deformations. Step 4 show the onset of macro-fault formation. (b and c) Inelastic axial strain measured at the strain gages as a function of the inelastic axial strain measured at the LVDTs for low (b) and high (c) injection rates. The color bar shows the pore fluid pressure. In such a plot, a slope of one means that both LVDTs and strain gages record the same deformation and that strain is accumulated in the bulk. However, a slope of zero indicates that the strain gages do not see the deformation seen by the LVDTs, which reveal that strain is localized (i.e., very probably accommodated through fault sliding). The different domains of deformation are segregated into the following categories: at $P_c - P_f \geq 80$ MPa deformation is ductile; at $80 \geq P_c - P_f \geq 60$ MPa deformation is typical of the brittle-ductile transition (BDT); at $P_c - P_f \leq 60$ MPa deformation is brittle; if the slope is unity, creep is occurring; if the slope is less than unity sliding on macroscopic fault is occurring. The steps 1 to 4 in panel (a) are represented in the panel b and c by the same colors.

In summary, in a ductile system, pore fluid pressure increase can switch the system to brittle deformation. However, the pore fluid pressure needs to remain high for a certain period of time/strain so that the micro-mechanical state of the rock evolves to a critical dilatancy state after which failure under macroscopic shearing can be induced. The importance of the rate at which the pore fluid pressure is raised can influence the final microstructural state of the rock mass (Figure 10a). Indeed, for low injection rates, the system remains at the pressure of the ductile-brittle transition for a longer period of time (Figure 10a), allowing for the development of transition deformations features (i.e., distributed shear zones) (stage 3 in Figure 10a) contributing to the damaging of the sample, lowering the creep phase required before sample macroscopic shear failure (stage 4 in Figure 10). However, high injection rates induce the transition from ductile to brittle mode of deformation without causing abundant damage (stage 3 in Figure 10a), forcing its creation during a creep phase at elevated pore fluid pressure (stage 4 in Figure 10a) to reach the macroscopic shear failure of the specimen.

Following recent data analysis methods (see Aubry et al., 2020; Meyer et al., 2019), strain partitioning between brittle and ductile deformations can be obtained by comparing the strain measured with the LVDTs and with the strain gages. This method helps in the differentiation between bulk deformation and sliding on a fault plane. Indeed, while the LVDTs are measuring the total axial strain, the strain gages (if not placed on the final macroscopic fault, otherwise they were not taken into account) are measuring the bulk strain but not the fault sliding that releases energy without storing strain in the surrounding bulk. By correcting

the strain from the elastic deformations (i.e., using the sample's Young's modulus), the inelastic axial strain (i.e., involving only microscopic damage) at the LVDTs and strain gages can be obtained. The slope of the inelastic axial strain measured at the strain gages as a function of the inelastic axial strain measured at the LVDTs allows for the differentiation between bulk deformations and macroscopic fault sliding (Figures 10b and 10c). A slope of unity indicates deformation occurring in the bulk of the sample, whereas a slope of zero indicates that deformations are localized and very probably accommodated by fault sliding. At low injection rates ($1 \text{ MPa} \cdot \text{min}^{-1}$) the onset of macroscopic fault sliding occurred before P_f attained 100 MPa (Figure 10b), while at high injection rates ($10 \text{ MPa} \cdot \text{min}^{-1}$) a bulk axial strain of about 0.3% was needed after P_f attained 100 MPa to reach the onset of fault sliding. These data highlight the importance of the damage history of rock masses regarding possible strain localization, fault formations and possible earthquake nucleation.

4.3. Implications for Deep Deformations and Earthquakes

Under crustal environments where ductile deformations are favored, pore fluid pressure variations are not rare. They can result from magma build-up in volcanic edifices, dyking, magmatic fluid pulses (e.g., Caricchi et al., 2011; Farquharson et al., 2016; Nishi et al., 1996) or fluid release during mineral phase changes (e.g., Moore & Vrolijk, 1992). We demonstrate that such pore fluid pressure increases would cause the brittle-ductile transition to migrate to greater depth, possibly leading to shear failure and seismicity at unexpected depths. This result is in agreement with field data suggesting that periods of elevated pore fluid pressures are responsible for ductile shear zones to be overprinted by brittle deformation (e.g., Marchesini et al., 2019; Prando et al., 2020; Wehrens et al., 2016).

In the context of ductile deep reservoir stimulation for geo-energy purposes (e.g., Asanuma et al., 2012; Bignall & Carey, 2011; Frioleifsson et al., 2014; Tsuchiya et al., 2015) our study suggests that injection would primarily produce dilation of the mass rock, possibly increasing its permeability and facilitating fluid circulation. However, the data presented here and previous studies on limestone suggest that porosity changes are relatively small in carbonates (e.g., Nicolas et al., 2017, 2016; Vajdova et al., 2004), inducing relatively small permeability variations (Meng et al., 2019). Additionally, operators should keep in mind that seismicity would never be suppressed in an initially ductile reservoir under fluid stimulation. Indeed, at such depth, rock permeability is low (Violay et al., 2015, 2017), requiring large permeability increases for viable exploitation. This would involve elevated pore fluid pressures for extensive periods of time which would certainly lead to shear failure of the reservoir and possibly to large-magnitude induced seismicity.

Additional experimental and numerical data are needed to better constrain the mechanics of such deep reservoirs. For example, the effect of temperature on the reservoir rock's mechanics could not be tested in our experiments. However, temperature has been shown to be a primordial parameter in brittle-ductile transition mechanics (e.g., Heard, 1960; Tullis & Yund, 1977). On the one hand, high temperature favors plastic mechanisms and ductile deformations. On the other hand, as long term injection may lower the in situ reservoir temperature, it may induce thermal cracking (e.g., Fredrich & Wong, 1986), or stress field variations (e.g., Fryer et al., 2020). A combination of the pore fluid pressure and temperature variations of deep crustal rocks must be studied for safe injections.

5. Conclusions

We conducted four constant pore fluid pressure experiments to constrain the brittle-ductile transition of Tavel limestone. Seven additional experiments with pore fluid pressure increase during the ductile deformation of Tavel limestone were performed. These new data provide new constraints on the role of pore fluid pressure variations at conditions close to and below the brittle-ductile transition:

- (1) In an initially ductile rock mass where deformations are controlled by compaction mechanisms, a pore fluid pressure build-up causes the system to instantaneously dilate due to micro-cracking of the rock.
- (2) Localized shear fracturing can develop in an initially ductile rock mass by mean of an increase of the pore fluid pressure. However, the localization is not instantaneous when the ductile to brittle transition is passed but is linked to the damage history of the rock sample. In the performed experiments, a transient creeping phase is necessary before macroscopic shear failure occurs.

- (3) A critical dilatancy (of about 1% for Tavel limestone) has to be reached in order to obtain shear failure of an initially ductile rock subjected to a pore fluid pressure increase.

Data Availability Statement

Raw data can be found at <https://zenodo.org/record/4268408#.X6wcs2hKiUk> (<https://doi.org/10.5281/zenodo.4268408>).

Acknowledgments

This work was funded by Gaznat SA (Grant FRICTION: Fault Reactivation during CO₂ sequestration). Marie Violay thanks the ERC project BEFINE (Grant 757290). The authors thank Baroz Gregoire from CIME laboratory (EPFL) for SEM technical assistance. François X. Passelègue thanks the Swiss National Science Foundation (Grant PZENP2/173613). The authors also thank Barnaby Fryer and Gabriel Meyer for proofreading. The authors thank the Carrières Lugan and Sébastien Violay for providing the rock samples. The authors thank the editor Y. Bernabe, associated editor A. Schubnel, along with M. Scuderi and one anonymous reviewer for their constructive comments.

References

- Asanuma, H., Muraoka, H., Tsuchiya, N., & Ito, H. (2012). The concept of the Japan Beyond-Brittle Project (JBBP) to develop EGS reservoirs in ductile zones. *Transactions - Geothermal Resources Council*, 36, 359–364.
- Ashby, M. F., & Sammis, C. G. (1990). The damage mechanics of brittle solids in compression. *Pure and Applied Geophysics*, 133(3), 489–521. <https://doi.org/10.1007/BF00878002>
- Aubry, J., Passelègue, F. X., Escartín, J., Gasc, J., Deldicque, D., & Schubnel, A. (2020). Fault stability across the seismogenic zone. *Journal of Geophysical Research: Solid Earth*, 125(8), e2020JB019670. <https://doi.org/10.1029/2020JB019670>
- Barton, N. (1976). The shear strength of rock and rock joints. *International Journal of Rock Mechanics and Mining Science & Geomechanics Abstracts*, 13(9), 255–279. [https://doi.org/10.1016/0148-9062\(76\)90003-6](https://doi.org/10.1016/0148-9062(76)90003-6)
- Bernabe, Y., & Brace, W. F. (1990). Deformation and fracture of berea sandstone. In A. Duba, W. Durham, J. Handin, & H. Wang (Eds.), *The brittle-ductile transition in rocks, volume 56, geophysical monograph series* (pp. 91–101). American Geophysical Union.
- Bignall, G., & Carey, B. (2011). A deep (5 km?) geothermal science drilling project for the Taupo Volcanic Zone—Who wants in?. In *33rd New Zealand geothermal workshop*. New Zealand.
- Brantut, N., Baud, P., Heap, M. J., & Meredith, P. G. (2012). Micromechanics of brittle creep in rocks. *Journal of Geophysical Research*, 117(B8). <https://doi.org/10.1029/2012JB009299>
- Byerlee, J. D. (1968). Brittle-ductile transition in rocks. *Journal of Geophysical Research*, 73(14), 4741–4750. <https://doi.org/10.1029/jb073i014p04741>
- Caricchi, L., Pommier, A., Pistone, M., Castro, J., Burgisser, A., & Perugini, D. (2011). Strain-induced magma degassing: Insights from simple-shear experiments on bubble bearing melts. *Bulletin of Volcanology*, 73(9), 1245–1257. <https://doi.org/10.1007/s00445-011-0471-2>
- Costin, L. S. (1983). A microcrack model for the deformation and failure of brittle rock. *Journal of Geophysical Research*, 88(B11), 9485–9492. <https://doi.org/10.1029/JB088iB11p09485>
- Costin, L. S. (1985). Damage mechanics in the post-failure regime. *Mechanics of Materials*, 4(2), 149–160. [https://doi.org/10.1016/0167-6636\(85\)90013-4](https://doi.org/10.1016/0167-6636(85)90013-4)
- Evans, B., Fredrich, J. T., & Wong, T.-F. (1990). The brittle-ductile transition in rocks' recent experimental and theoretical progress. In A. G. Duba, W. B. Durham, J. W. Handin, & H. F. Wang, (Eds.), *The brittle-ductile transition in rocks*. AGU. <https://doi.org/10.1029/GM056p0001>
- Evans, B., & Kohlstedt, D. L. (1995). Rock physics & phase relations: A handbook of physical constants, *Rheology of Rocks*, 3, 148–165. <https://doi.org/10.1029/RF003p0148>
- Farquharson, J., Heap, M. J., Baud, P., Reuschlé, T., & Varley, N. R. (2016). Pore pressure embrittlement in a volcanic edifice. *Bulletin of Volcanology*, 78(1), 6. <https://doi.org/10.1007/s00445-015-0997-9>
- Farver, J. R., & Yund, R. A. (1991). Oxygen diffusion in quartz: Dependence on temperature and water fugacity. *Chemical Geology*, 90(1–2), 55–70. [https://doi.org/10.1016/0009-2541\(91\)90033-N](https://doi.org/10.1016/0009-2541(91)90033-N)
- Fredrich, J. T., Evans, B., & Wong, T. (1989). Brittle to plastic transition in Carrara Marble. *Journal of Geophysical Research*, 94(B4), 4129–4145. <https://doi.org/10.1029/JB094iB04p04129>
- Fredrich, J. T., & Wong, T. F. (1986). Micromechanics of thermally induced cracking in three crustal rocks. *Journal of Geophysical Research*, 91(B12), 12743–12764. <https://doi.org/10.1029/JB091iB12p12743>
- Frioleifsson, G. O., Elders, W. A., & Albertsson, A. (2014). The concept of the Iceland deep drilling project. *Geothermics*, 49, 2–8. <https://doi.org/10.1016/j.geothermics.2013.03.004>
- Fryer, B., Siddiqi, G., & Laloui, L. (2020). Injection-induced seismicity: Strategies for reducing risk using high stress path reservoirs and temperature-induced stress preconditioning. *Geophysical Journal International*, 220(2), 1436–1446. <https://doi.org/10.1093/gji/ggj490>
- Goetze, C., & Brace, W. F. (1972). *Laboratory observations of high-temperature rheology of rocks*. In *Developments in Geotectonics: The Upper Mantle* (pp. 583–600). Elsevier Publishing Company. <https://doi.org/10.1016/B978-0-444-41015-3.50036-7>
- Goetze, C., & Evans, B. (1979). Stress and temperature in the bending lithosphere as constrained by experimental rock mechanics. *Geophysical Journal of the Royal Astronomical Society*, 59(3), 463–478. <https://doi.org/10.1111/j.1365-246X.1979.tb02567.x>
- Griggs, D. (1967). Hydrolytic weakening of quartz and other silicates. *Geophysical Journal of the Royal Astronomical Society*, 14(1–4), 19–31. <https://doi.org/10.1111/j.1365-246X.1967.tb0218.x>
- Guéguen, Y., & Palciauskas, V. (1994). *Introduction to the physics of rocks*. Princeton University Press.
- Handin, J., Hager, R. V. J., Friedman, M., & Feather, J. N. (1963). Experimental deformation of sedimentary rocks under confining pressure: Pore pressure tests. *American Association of Petroleum Geologists*, 47(5), 717–755.
- Handy, M. R., Hirth, G., & Bürgmann, R. (2007). Continental fault structure and rheology from the frictional-to-viscous transition downward. In N. Handy, M. R., G. Hirth, & Hovius, (Eds.), *Tectonic faults: Agents of change on a dynamic Earth* (pp. 139–182). MIT Press. <https://doi.org/10.7551/mitpress/6703.003.0008>
- Heard, H. C. (1960). Transition from brittle fracture to ductile flow in Solnhofen limestone as a function of temperature, confining pressure, and interstitial fluid pressure. In D. Griggs, & J. Handin, (Eds.), *Rock deformation* (pp. 193–226). Geological Society of America Memoirs.
- Kaproth, B. M., & Marone, C. (2013). Slow earthquakes, preseismic velocity changes, and the origin of slow frictional stick-slip. *Science*, 341(6151), 1229–1232. <https://doi.org/10.1126/science.1239577>
- Kohlstedt, D. L., Evans, B., & Mackwell, S. J. (1995). Strength of the lithosphere: Constraints imposed by laboratory experiments. *Journal of Geophysical Research*, 100(B9), 17587–17602. <https://doi.org/10.1029/95JB01460>

- Kranz, R. L., & Scholz, C. H. (1977). Critical dilatant volume of rocks at the onset of tertiary creep. *Journal of Geophysical Research*, 82(30), 4893–4898. <https://doi.org/10.1029/JB082i030p04893>
- Lockner, D. A. (1995). Rock Physics & Phase Relations: A Handbook of Physical Constants. *Rock Failure*, 3, 127–147. <https://doi.org/10.1029/RF003p0127>
- Marchesini, B., Garofalo, P. S., Menegon, L., Mattila, J., & Viola, G. (2019). Fluid-mediated, brittle-ductile deformation at seismogenic depth - Part 1: Fluid record and deformation history of fault veins in a nuclear waste repository (Olkiluoto Island, Finland). *Solid Earth*, 10(3), 809–838. <https://doi.org/10.5194/se-10-809-2019>
- Maurer, W. C. (1965). Shear failure of rock under compression. *Society of Petroleum Engineers Journal*, 5(2), 167–176. <https://doi.org/10.2118/1054-pa>
- Meng, F., Baud, P., Ge, H., & Wong, T. (2019). The effect of stress on limestone permeability and effective stress behavior of damaged samples. *Journal of Geophysical Research: Solid Earth*, 124(1), 376–399. <https://doi.org/10.1029/2018JB016526>
- Meyer, G. G., Brantut, N., Mitchell, T. M., & Meredith, P. G. (2019). Fault reactivation and strain partitioning across the brittle-ductile transition. *Geology*, 47(12), 1127–1130. <https://doi.org/10.1130/G46516.1>
- Mogi, K. (1974). On the pressure dependence of strength of rocks and the Coulomb fracture criterion. *Tectonophysics*, 21(3), 273–285. [https://doi.org/10.1016/0040-1951\(74\)90055-9](https://doi.org/10.1016/0040-1951(74)90055-9)
- Moore, J. C., & Vrolijk, P. (1992). Fluids in accretionary prisms. *Reviews of Geophysics*, 30(2), 112–135. <https://doi.org/10.1029/92RG00201>
- Murrell, S. A. F. (1967). The effects of triaxial stress systems on the fracture of rocks, and on the nature of faulting and earthquakes. *Geophysical Journal International*, 14(1–4), 81–87. <https://doi.org/10.1111/j.1365-246X.1967.tb06226.x>
- Nicolas, A., Fortin, J., Regnet, J. B., Dimanov, A., & Guéguen, Y. (2016). Brittle and semi-brittle behaviors of a carbonate rock: Influence of water and temperature. *Geophysical Journal International*, 206(1), 438–456. <https://doi.org/10.1093/gji/ggw154>
- Nicolas, A., Fortin, J., Regnet, J. B., Verberne, B. A., Plümper, O., Dimanov, A., et al. (2017). Brittle and semibrittle creep of Tavel limestone deformed at room temperature. *Journal of Geophysical Research: Solid Earth*, 122, 1–24. <https://doi.org/10.1002/2016JB013557>
- Nishi, Y., Sherburn, S., Scott, B. J., & Sugihara, M. (1996). High-frequency earthquakes at White Island volcano, New Zealand: Insights into the shallow structure of a volcano-hydrothermal system. *Journal of Volcanology and Geothermal Research*, 72(3–4), 183–197. [https://doi.org/10.1016/0377-0273\(96\)00005-4](https://doi.org/10.1016/0377-0273(96)00005-4)
- Niu, F., Silver, P. G., Daley, T. M., Cheng, X., & Majer, E. L. (2008). Preseismic velocity changes observed from active source monitoring at the Parkfield SAFOD drill site. *Nature*, 454(7201), 204–208. <https://doi.org/10.1038/nature07111>
- Noël, C., Passelègue, F. X., Giorgetti, C., & Violay, M. (2019). Fault reactivation during fluid pressure oscillations: Transition from stable to unstable slip. *Journal of Geophysical Research: Solid Earth*, 124(11), 10940–10953. <https://doi.org/10.1029/2019JB018517>
- Noël, C., Pimienta, L., & Violay, M. (2019). Time-dependent deformations of sandstone during pore fluid pressure oscillations: Implications for natural and induced seismicity. *Journal of Geophysical Research: Solid Earth*, 124(1), 801–821. <https://doi.org/10.1029/2018JB016546>
- Ougier-Simonin, A., & Zhu, W. (2013). Effects of pore fluid pressure on slip behaviors: An experimental study. *Geophysical Research Letters*, 40(11), 2619–2624. <https://doi.org/10.1002/grl.50543>
- Paterson, M. S. (1958). Experimental deformation and faulting in Wombeyan marble. *Geological Society of America Bulletin*, 69(4), 465–476. [https://doi.org/10.1130/0016-7606\(1958\)69\[465:EDAFIW\]2.0.CO;2](https://doi.org/10.1130/0016-7606(1958)69[465:EDAFIW]2.0.CO;2)
- Pimienta, L., Sarout, J., Esteban, L., David, C., & Clennell, M. B. (2017). Pressure-dependent elastic and transport properties of porous and permeable rocks: Microstructural control. *Journal of Geophysical Research: Solid Earth*, 122(11), 8952–8968. <https://doi.org/10.1002/2017JB014464>
- Prando, F., Menegon, L., Anderson, M., Marchesini, B., Mattila, J., & Viola, G. (2020). Fluid-mediated, brittle-ductile deformation at seismogenic depth – Part 2: Stress history and fluid pressure variations in a shear zone in a nuclear waste repository (Olkiluoto Island, Finland). *Solid Earth*, 11, 489–511. <https://doi.org/10.5194/se-11-489-2020>
- Renard, F., Gratier, J. P., & Jamtveit, B. (2000). Kinetics of crack-sealing, intergranular pressure solution, and compaction around active faults. *Journal of Structural Geology*, 22(10), 1395–1407. [https://doi.org/10.1016/S0191-8141\(00\)00064-X](https://doi.org/10.1016/S0191-8141(00)00064-X)
- Robinson, L. H. J. (1959). Effect of pore and confining pressures on failure characteristics of sedimentary rocks. *Society of Petroleum Engineers*, 216, 26–32.
- Rutter, E. H. (1972a). The effects of strain-rate changes on the strength and ductility of Solnhofen limestone at low temperatures and confining pressures. *International Journal of Rock Mechanics and Mining Sciences*, 9(2), 183–189. [https://doi.org/10.1016/0148-9062\(72\)90020-4](https://doi.org/10.1016/0148-9062(72)90020-4)
- Rutter, E. H. (1972b). The influence of interstitial water on the rheological behavior of calcite rocks. *Tectonophysics*, 14(1), 13–33. [https://doi.org/10.1016/0040-1951\(72\)90003-0](https://doi.org/10.1016/0040-1951(72)90003-0)
- Rutter, E. H. (1986). On the nomenclature of mode of failure transitions in rocks. *Tectonophysics*, 122(3–4), 381–387. [https://doi.org/10.1016/0040-1951\(86\)90153-8](https://doi.org/10.1016/0040-1951(86)90153-8)
- Sammis, C. G., & Ashby, M. F. (1986). The failure of brittle porous solids under compressive stress states. *Acta Metallurgica*, 34(3), 511–526. [https://doi.org/10.1016/0001-6160\(86\)90087-8](https://doi.org/10.1016/0001-6160(86)90087-8)
- Sarout, J., & Guéguen, Y. (2008a). Anisotropy of elastic wave velocities in deformed shales: Part 1 — Experimental results. *Geophysics*, 73(5), D75. <https://doi.org/10.1190/1.2952745>
- Sarout, J., & Guéguen, Y. (2008b). Anisotropy of elastic wave velocities in deformed shales: Part 2 — Modeling results. *Geophysics*, 73(5), D75. <https://doi.org/10.1190/1.2952745>
- Scholz, C. H. (2019). *The mechanics of earthquakes and faulting*. Cambridge University Press. <https://doi.org/10.1017/9781316681473>
- Schubnel, A., Walker, E., Thompson, B. D., Fortin, J., Guéguen, Y., & Young, R. P. (2006). Transient creep, aseismic damage and slow failure in Carrara marble deformed across the brittle-ductile transition. *Geophysical Research Letters*, 33(17). <https://doi.org/10.1029/2006GL026619>
- Scuderi, M. M., Marone, C., Tinti, E., Di Stefano, G., & Collettini, C. (2016). Precursory changes in seismic velocity for the spectrum of earthquake failure modes. *Nature Geoscience*, 9, 695–700. <https://doi.org/10.1038/ngeo2775>
- Shreedharan, S., Bolton, D. C., Rivière, J., & Marone, C. (2021). Competition between preslip and deviatoric stress modulates precursors for laboratory earthquakes. *Earth and Planetary Science Letters*, 553, 116623. <https://doi.org/10.1016/j.epsl.2020.116623>
- Sibson, R. H. (1977). Fault rocks and fault mechanisms. *Journal of the Geological Society*, 133(3), 191–213. <https://doi.org/10.1144/gsjgs.133.3.0191>

- Sibson, R. H. (1982). Fault zone models, heat flow, and the depth distribution of earthquakes in the continental crust of the United States. *Bulletin of the Seismological Society of America*, 72, 151–163.
- Taira, T., Brenguier, F., & Kong, Q. (2015). Ambient noise-based monitoring of seismic velocity changes associated with the 2014 Mw 6.0 South Napa earthquake. *Geophysical Research Letters*, 42(17), 6997–7004. <https://doi.org/10.1002/2015GL065308>
- Tenthorey, E., Cox, S. F., & Todd, H. F. (2003). Evolution of strength recovery and permeability during fluid-rock reaction in experimental fault zones. *Earth and Planetary Science Letters*, 206(1–2), 161–172. [https://doi.org/10.1016/S0012-821X\(02\)01082-8](https://doi.org/10.1016/S0012-821X(02)01082-8)
- Tsuchiya, N., Asanuma, H., Okamoto, A., Sakaguchi, K., Hirano, N., Kizaki, A., & Watanabe, N. (2015). Fundamental study for beyond brittle geothermal reservoirs. In *Proceedings world geothermal congress* (pp. 19–25). Australia.
- Tullis, J., & Yund, R. A. (1977). Experimental deformation of dry westerly granite. *Journal of Geophysical Research*, 82(36), 5705–5718. <https://doi.org/10.1029/JB082i036p05705>
- Tullis, J., & Yund, R. A. (1980). Hydrolytic weakening of experimentally deformed Westerly granite and Hale albite rock. *Journal of Structural Geology*, 2(4), 439–451. [https://doi.org/10.1016/0191-8141\(80\)90005-X](https://doi.org/10.1016/0191-8141(80)90005-X)
- Vajdova, V., Baud, P., & Wong, T. (2004). Compaction, dilatancy, and failure in porous carbonate rocks. *Journal of Geophysical Research*, 109(B5). <https://doi.org/10.1029/2003JB002508>
- Vajdova, V., Zhu, W., Natalie Chen, T. M., & Wong, T. (2010). Micromechanics of brittle faulting and cataclastic flow in Tavel limestone. *Journal of Structural Geology*, 32(8), 1158–1169. <https://doi.org/10.1016/j.jsg.2010.07.007>
- Vincké, O., Boutéca, M. J., Piau, J. M., & Fourmaintraux, D. (1998). Study of the effective stress at failure. In J.-F. Thimus, Y. Abousleiman, A. H.-D. Cheng, O. Coussy, & E. Detournay, (Eds.), *Poromechanics, A tribute to Maurice A. Biot* (pp. 635–639). Rotterdam.
- Violay, M., Gibert, B., Mainprice, D., & Burg, J. P. (2015). Brittle versus ductile deformation as the main control of the deep fluid circulation in oceanic crust. *Geophysical Research Letters*, 42(8), 2767–2773. <https://doi.org/10.1002/2015GL063437>
- Violay, M., Gibert, B., Mainprice, D., Evans, B., Dautria, J. M., Azais, P., & Pezard, P. (2012). An experimental study of the brittle-ductile transition of basalt at oceanic crust pressure and temperature conditions. *Journal of Geophysical Research*, 117(B3). <https://doi.org/10.1029/2011JB008884>
- Violay, M., Heap, M. J., Acosta, M., & Madonna, C. (2017). Porosity evolution at the brittle-ductile transition in the continental crust: Implications for deep hydro-geothermal circulation. *Scientific Reports*, 7(1).7705. <https://doi.org/10.1038/s41598-017-08108-5>
- von Kármán, T. (1911). Festigkeitsversuche unter allseitigem Druck. *Verein Deutsch Ing*, 55, 1749–1757.
- Wang, X. Q., Schubnel, A., Fortin, J., Guéguen, Y., & Ge, H. K. (2013). Physical properties and brittle strength of thermally cracked granite under confinement. *Journal of Geophysical Research: Solid Earth*, 118(12), 6099–6112. <https://doi.org/10.1002/2013JB010340>
- Wang, Y., Meng, F., Wang, X., Baud, P., & Wong, T. F. (2018). Effective stress law for the permeability and deformation of four porous limestones. *Journal of Geophysical Research: Solid Earth*, 123(6), 4707–4729. <https://doi.org/10.1029/2018JB015539>
- Weertman, J. (1978). Creep laws for the mantle of the Earth. *Philosophical Transactions of the Royal Society of London - Series A: Mathematical and Physical Sciences*, 288(1350), 9–26. <https://doi.org/10.1098/rsta.1978.0003>
- Wehrens, P., Berger, A., Peters, M., Spillmann, T., & Herwegh, M. (2016). Deformation at the frictional-viscous transition: Evidence for cycles of fluid-assisted embrittlement and ductile deformation in the granitoid crust. *Tectonophysics*, 693, 66–84. <https://doi.org/10.1016/j.tecto.2016.10.022>
- Wei, Y., & Anand, L. (2008). On micro-cracking, inelastic dilatancy, and the brittle-ductile transition in compact rocks: A micro-mechanical study. *International Journal of Solids and Structures*, 45(10), 2785–2798. <https://doi.org/10.1016/j.ijsolstr.2007.11.028>
- Wong, T., & Baud, P. (2012). The brittle-ductile transition in porous rock: A review. *Journal of Structural Geology*, 44, 25–53. <https://doi.org/10.1016/j.jsg.2012.07.010>
- Wong, T., David, C., & Zhu, W. (1997). The transition from brittle faulting to cataclastic flow in porous sandstones: Mechanical deformation. *Journal of Geophysical Research*, 102(B2), 3009–3025. <https://doi.org/10.1029/96JB03282>
- Zhu, W., Baud, P., & Wong, T. (2010). Micromechanics of cataclastic pore collapse in limestone. *Journal of Geophysical Research*, 115(B4). <https://doi.org/10.1029/2009JB006610>